Electronic Supplementary Material of

High-Throughput Underwater Elemental Analysis μJ-Laser-Induced Breakdown Spectroscopy at kHz Repetition Rate: Part I, Ultrasound-Enhanced Optical Emission Spectroscopy Towards Application Perspectives

Boyang Xue[1, 2], Yi You[2†], Igor Gornushkin[2], Ronger Zheng[1] and Jens Riedel[21] Ocean University of China, Qingdao, Shandong 266100, China

[2] Federal Institute for Materials Research and Testing (BAM), Berlin D-12489, Germany
[†]Corresponding Author: Yi You, Email: yi.you@bam.de, Tel: +49-30-81405542

1. Experimentally measured laser energy under different repetition-rates

The laser-pulse energy under different repetition rates was measured with a fast-response photodiode (DET210, Thorlabs, Dachau, Germany) directly connected to an oscilloscope (DL9140, 5 GS/s, 1 GHz, Yokogawa, Musashino, Japan). In the present work, the oscilloscope was configured to four-channel mode, which allowed a maximum sample rate at 2.5 GS/s. Namely, the temporal resolution was at 4×10^{-10} s, *i.e*. 0.4 ns. The laser was not focused and was directed towards a white dull paper-based surface. The piece of paper was mounted to an aluminum-alloy heat sink to dump the thermal energy from the laser. The diffusive reflection from this surface was then collected by the photodiode. Several neutral density filters were used in front of the detector to attenuate the laser intensity.

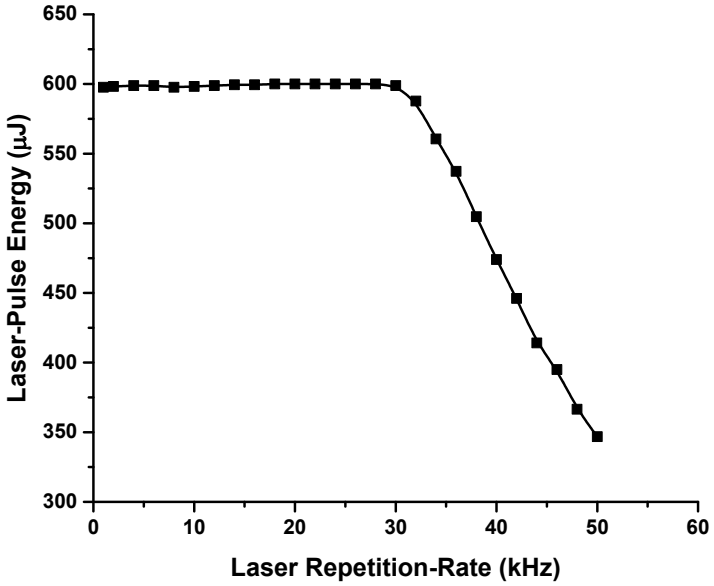

Figure S 1. Laser-pulse energy as a function of the laser repetition-rate.

The per-pulse energy remains near-constant in the range of 1 Hz to ~32 kHz (*cf*. Figure S1). Thereafter, the energy decreased monotonically in a near linear fashion. Close inspection revealed that the per-pulse energy output follows a sigmoid function. The energy-output behavior of this laser is beyond the scope of this work. Within the range of the repetition rate used in this study, the per-pulse laser energy was considered constant.

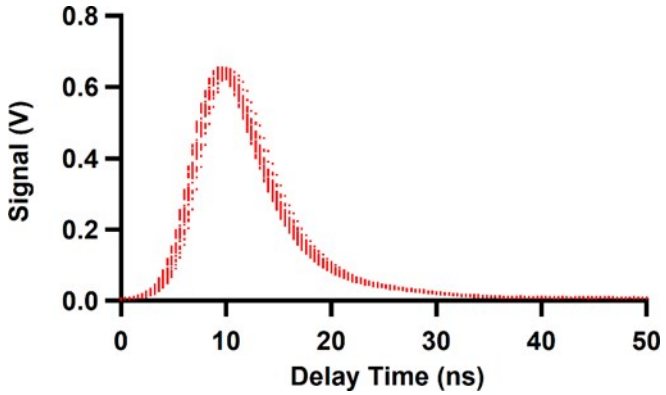

Figure S 2. Transient laser profile from 10 Hz to 30 kHz. The dots are the oscilloscope signals for each repetition rate.

In addition to the energy profile, the transient laser intensity was also measured with the same setup from 10 Hz to 30 kHz. To demonstrate the temporal stability of the laser, the transient profiles of the laser within the repetition-rate range were stacked in Figure S2. Further, we affirmed that the laser profile, especially the full-width half maximum (FWHM) remains unchanged within the repetition rate covered in this work (*cf*. Figure S3). Specifically, the variations in FWHM are due to the digitizing error of the oscilloscope, where the minimal time step between two datapoints is 0.4 ns at 2.5 GSa/s. Similar assessment was also performed for the start time of each lasing event. The Q-switch jitter was also within 0.4 ns (*cf*. Figure S4).

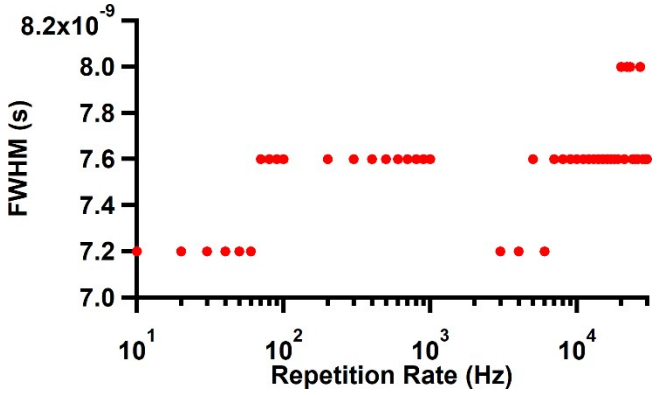

Figure S 3. FWHM of the transient laser profile with respect to repetition rates.

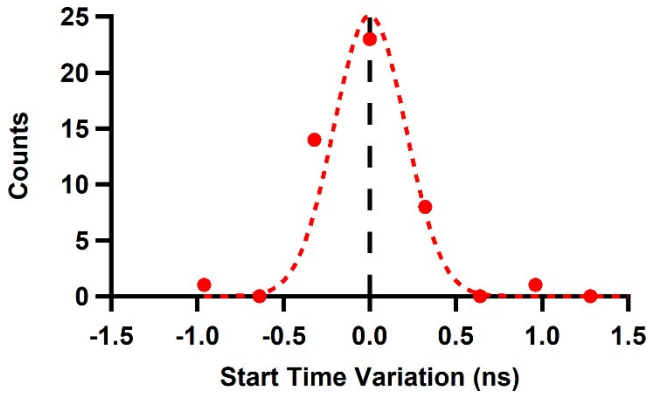

Figure S 4. Histogram of the variation of laser start-time (Jitter).

2. Determination of magnification factor

The magnification factor was measured with a standard needle with an outer diameter of 450 µm. The size of the iCCD pixel (iStar DH 734i, ANDOR Technology Ltd., Belfast, UK) is 13 µm. An image of the needle with the acquisition optics was taken (*cf*. Figure S5). The distance between the edges was found to be 705 pixels. As such, the magnification factor was about 20x, corresponding to a resolution of 0.638 µm /pixel.

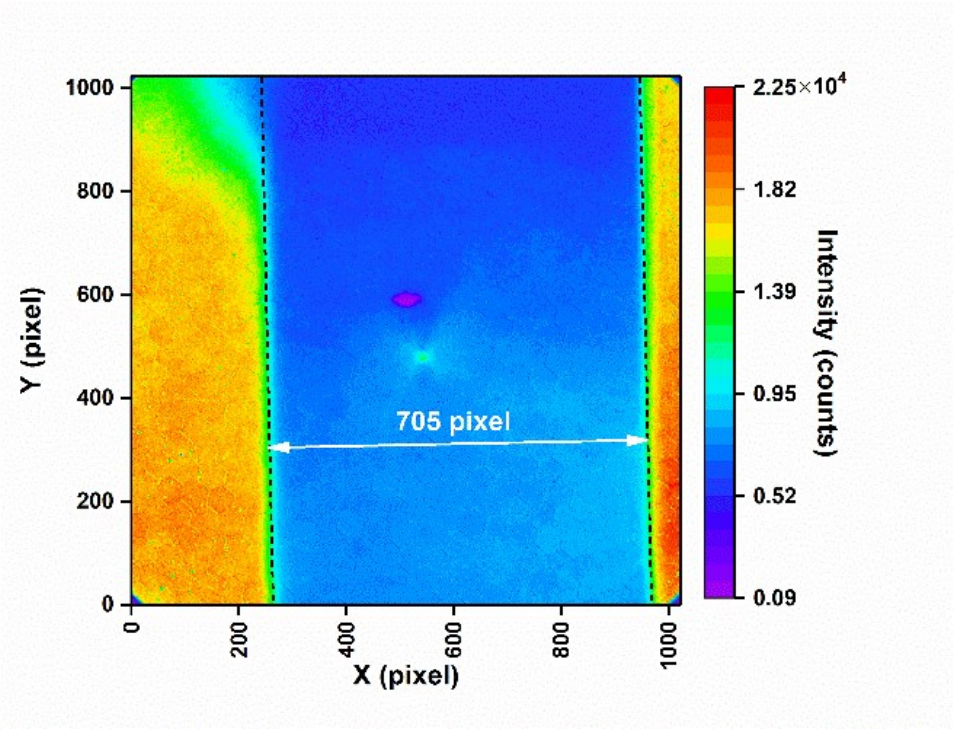

Figure S 5. Image of a needle with an outer diameter of 450 µm. The black dashed lines are the edges found by image processing. The white arrowed line shows the pixel distance between the two edge lines.

To acquire the correct pixel number between the two edges of the reference needle, the image was first processed with edge detection. The edge points provided a rough estimation to register the

edges. Subsequently, two lines were used to fit those points at the edges. Notably, a constrain to ensure the slopes of the lines was used to acquire parallel line fittings. The distance was then determined by calculating the distance between the fitted lines. The position of the white-arrowed line was arbitrarily chosen in this case.

3. Temporal evolution of the plasma emission

The temporal evolutions of the spectral emissions in the range from 300 nm to 850 nm were investigated by an Echelle spectrometer equipped with an iCCD (Butterfly, LTB GmbH, Berlin, Germany) as the detector. During the initial period of plasma growth from 0 to 39 ns, the photocathode was gated at 4 ns with a step size of 1 ns. For the latter period during 20 to 110 ns, where the plasma became weaker and with slower progression, the photocathode was then gated at 10 ns with a step of 5 ns. The zero-point of the time delay was set at the moment at which the plasma was initially ignited. The exposure time of the iCCD was both set as 10 s, and the MCP gain was fixed at 3000 (maximal gain is 4096 on this iCCD).

From the temporal evolution of the spectral emission, it was observed that the elemental lines became distinguishable at the delay of 28 ns after the laser firing signal, while the broadband continuum emission persisted up to the delay of 40 ns (*cf*. Figure S6). Thus, in the following spectral and imaging investigations with respect to different operating conditions of the laser, the gate delay was maintained at 28ns with a gate width of 1000 ns to include all the information of characteristic lines including the broadband emission. While for evaluating the analytical performance of the DPSS-LIBS system, a gate delay of 40 ns and a gate width of 1000 ns were used to ensure optimized signal-to-background ratio (SBR, *cf*. Figure S7).

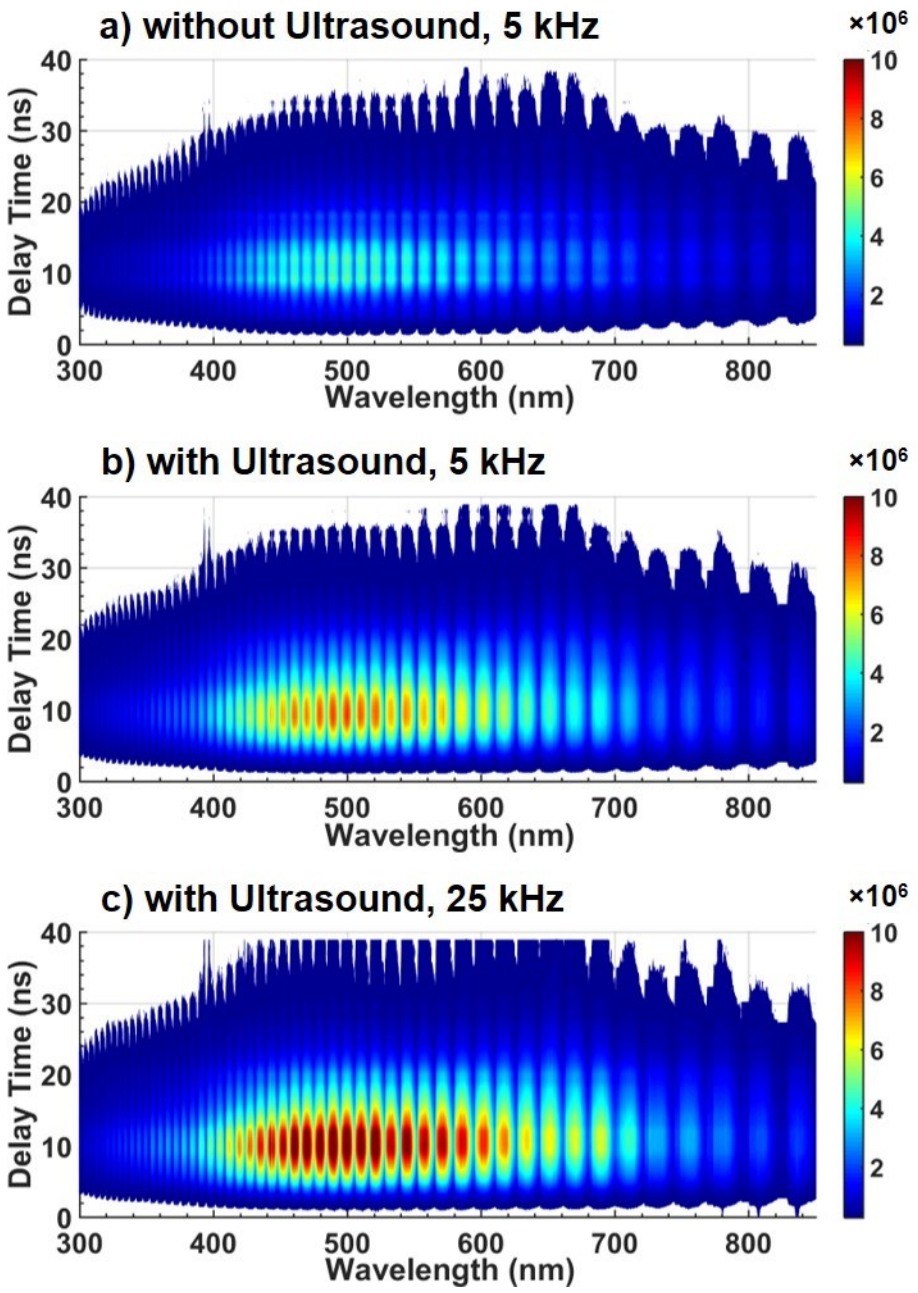

Figure S 6. Temporal evolution of the spectral emissions from 0 ns to 39 ns obtained without ultrasound at the repetition-rate of 5 kHz (a), with ultrasound at 5 kHz (b), and with ultrasound at 25 kHz (c), respectively.

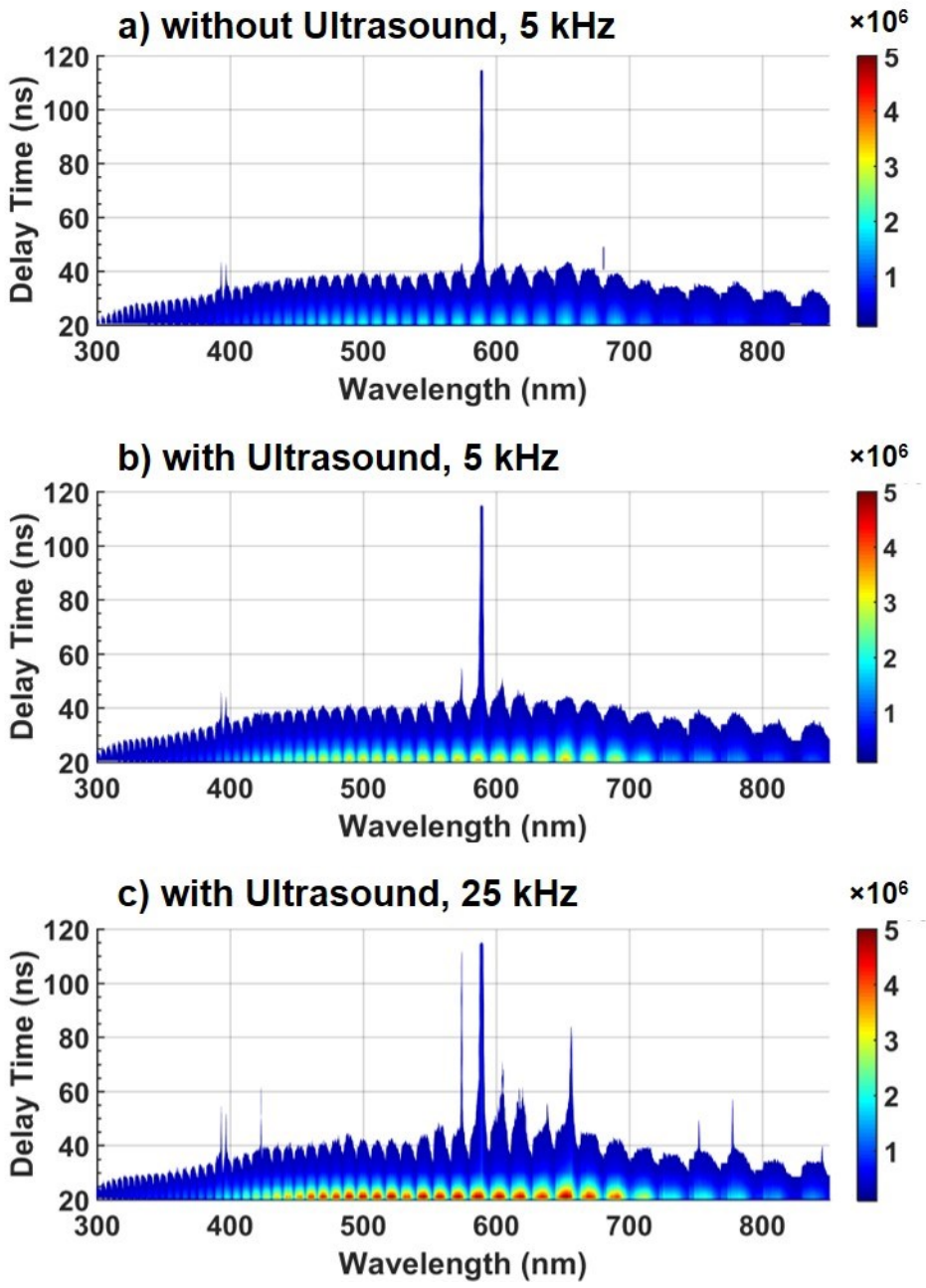

Figure S 7. Temporal evolution of the spectral emissions from 20 ns to 110 ns obtained without ultrasound at the repetition-rate of 5 kHz (a), with ultrasound at 5 kHz (b), and with ultrasound at 25 kHz (c), respectively.

4. Schematic of the coupling between the near-field ultrasound and laser-induced plasma

The location of the sonotrode was carefully aligned to obtain the optimal plasma emission, which relies upon visual and audible inspections. Specifically, the horn with a width of 8.0 mm, was centered 12.1 mm away from the wall of the sample container (*cf*. Figure S8). The horizontal

distance between the horn-center and the laser focal point was 5.3 mm, while the vertical distance was 7.0 mm (as denoted in Figure S8). Such an alignment allows the near-field ultrasonic radiation to cover the laser focal region. The laser transmission distance in water was estimated to be 6.8 mm here, considering the refractions by the quartz and the water. This distance was measured from picture taken for the side view with a digital camera.

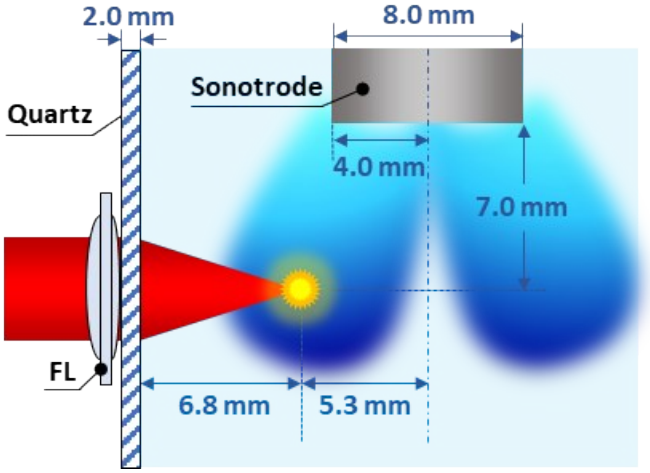

Figure S 8. Side view of the specific locations of the sonotrode and the laser focus.

The intensity of the ultrasound wave is not homogeneous neither temporally nor spatially. It is time-dependent with alternating compression and rarefaction cycles, and space-dependent with the ridge and the trough of wave. Hypothetically, the temporal synchronization as well as the spatial coupling between the ultrasound and the laser should to be essential for the enhancement of underwater breakdown. By synchronizing the ultrasound and the laser-pulse with different insertion delays, it was found that the timing sequence exhibited no obvious effects on the plasma emission intensities (data not shown). The results demonstrated that the phase matching and even pulse synchronizing between the ultrasound and the laser-pulse were unnecessary in the present study. Although the transient ultrasound has a compression and rarefaction cycle of only 25 μs (40 kHz), the overall effect of ultrasound may appear to be stationary to the laser plasma. The material used for the tank, quartz, is considered a sound-hard surface, where majority of the acoustic radiation bounces back into the medium. In this case, the quartz tank itself resembles a resonance cavity. Very similar to a transducer-reflector setup in acoustic traps, the ultrasonic force-field appear to be stationary. Thus, it becomes less critical for temporal synchronization in this case.

Different from the temporal irrelevance, it was found that the signal enhancement strongly depended on the relative position of the laser focus with respect to the horn. Notably, the plasma enhancement was most significant in the near-field region. To further investigate the effects of the spatial coupling with the near-field ultrasound, we compared the spectral emissions obtained with different horizontal positions of the laser focus relative to the horn. In practice, the previously employed focusing lens of f=8 mm was too short to cover the near-field region of the horn, which was centered 12.1 mm away from the tank-wall. Thus, the f=15 mm focusing lens was chosen to provide an enough range of laser-transmission distance in water. Moreover, the f=15 mm focusing lens with larger numerical aperture and wider beam waist, cannot initialize the breakdown independently without ultrasound. Thus, the plasma emission appeared to be more sensitive to the

presence of ultrasound. Here, we define the inner surface of the quartz tank on the laser side as the origin (*cf.* Figure S8). It was observed that maximal emissions occurred at 8 mm, which was aligned with the edge of the sonotrode on the laser side. To demonstrate the spatially dependent enhancements, we chose Ca I, O I and continuum emission (at 500 nm) as examples (*cf.* Figure S9). The maximal intensities occurred near the left edge of the sonotrode at f=8 mm for all three species. Further moving the plasma towards the right-hand-side (RHS) resulted in decreasing in emission intensities for the three emitters. This result suggested that the ultrasonic force-field is significantly lower at the sonotrode center in comparison to the edges. This decrease in emission intensities can be attributed to the inhomogeneous distribution of acoustic radiation depending on the geometry of the sonotrode. Thereafter, moving the plasma more towards the RHS caused the emission intensities to increase again. The plasma emission was enhanced by moving the plasma from the sonotrode center towards to the far edge. However, due to the attenuation of laser energy by the medium, the emission intensity was significantly lower on the far edge comparing to the near one.

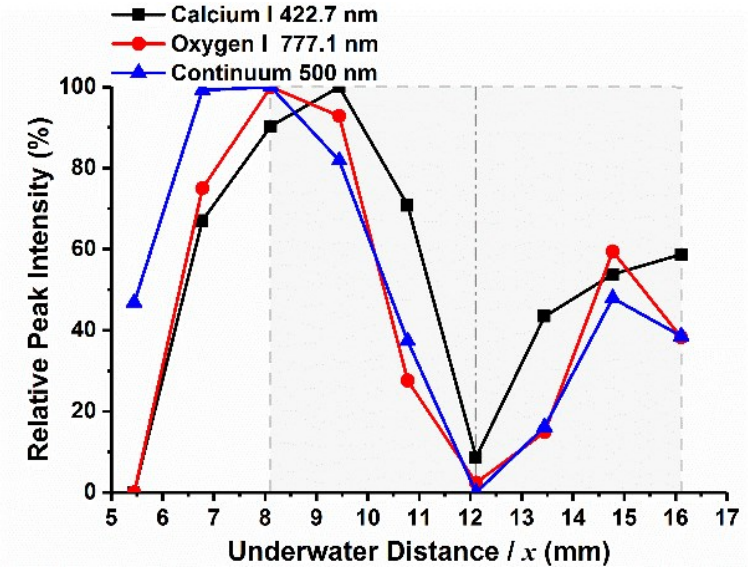

Figure S 9. Normalized peak intensities of atomic calcium at 422.7 nm, atomic oxygen at 777.1 nm and continuum emissions at 500 nm, as a function of underwater transmission distance of the laser beam. Here the underwater distance was estimated with the consideration of the refractive index of water. The shadow represented the horizontal coverage of the sonotrode, with the center located at 12 mm (gray dot-dashed trace) and edges at 8 mm and 16 mm (gray dashed trace). The plasmas were generated at the laser repetition-rate of 30 kHz, and with the f=15 mm focusing lens. The spectra were recorded with the exposure time of 20 s, at a gate delay time of 28 ns and with a gate width of 1000 ns. The sample was a standard aqueous solution containing 600 µg /mL Ca^{2+} and 200 µg /mL Na^{+}.

In addition to the general trend of the spatial profile of plasma emission, careful inspection revealed that the different species reached their maximal intensities slightly different from another (*cf.* Figure S9, solid traces between 6-9 mm). In specific, the maximal emissions of continuum emission, O I and Ca I occurred at 6.5 mm, 8 mm, and 9.5 mm respectively. This trend implied that even at the area where near-field ultrasound presents, the slight inhomogeneity of the force field may impact different species in quite unique ways. The use of this chemical information encoded in spatial domain will be explored in a future publication.

5. Schlieren imaging for viewing the thermal lens effect

In order to visualize the thermal lens effect, which prevent plasm formation at low repetition rates without external perturbation (*e.g.*, ultrasound), schlieren images were recorded with the optical geometry shown in Figure S10. Briefly, the 1064 nm laser was focused into a quartz cuvette with an optical depth of 10 mm. Another laser operating in continuous-wave (CW) mode at 532 nm was used to illuminate the sampling volume containing the plasma ignition site. To improve the sensitivity of this schlieren platform, the laser beam was expanded through a two-lens system with a pin hole at the intermediate focusing point. To record the image, a CMOS imaging sensor (EO5012M, Edmund Optics) was operated in free-run mode.

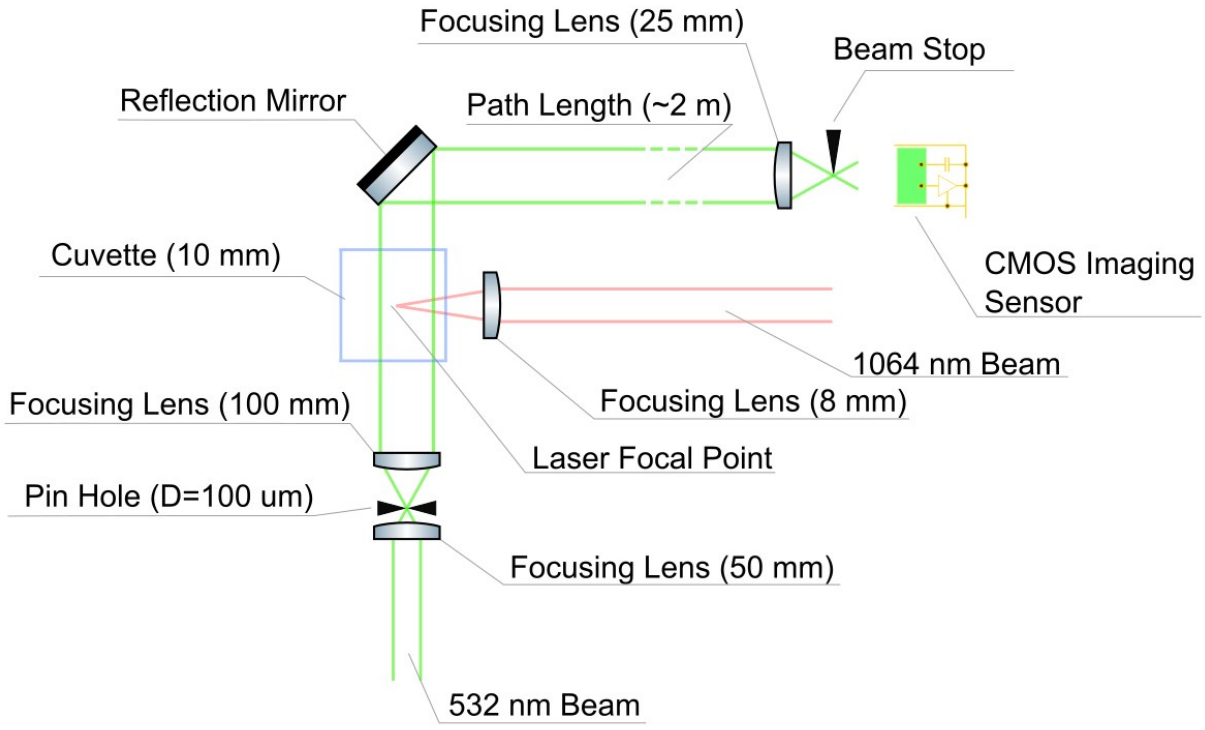

Figure S 10. Top-view schematic of schlieren imaging setup.

The resulting schlieren image showed significant heat accumulation (*cf*. Figure S11). Note that the bright spot at/near the laser (1064 nm) focal point was not related to laser-induced plasma. Instead, it was merely due to the change of refractive index due to thermal accumulation. Similar effect can be seen along the excitation beam path. Interestingly, the laser beam profile and the laser focus were both optimized. Namely, the photon density should be horizontally symmetric. In fact, if the laser and focusing lens was not concentrically aligned, plasma cannot be ignited due to the low pulse energy of 600 μJ/pulse. However, significant change of refractive index was only observed below the focal point. Up to this point, we were not able to deduce the reason for such an observation.

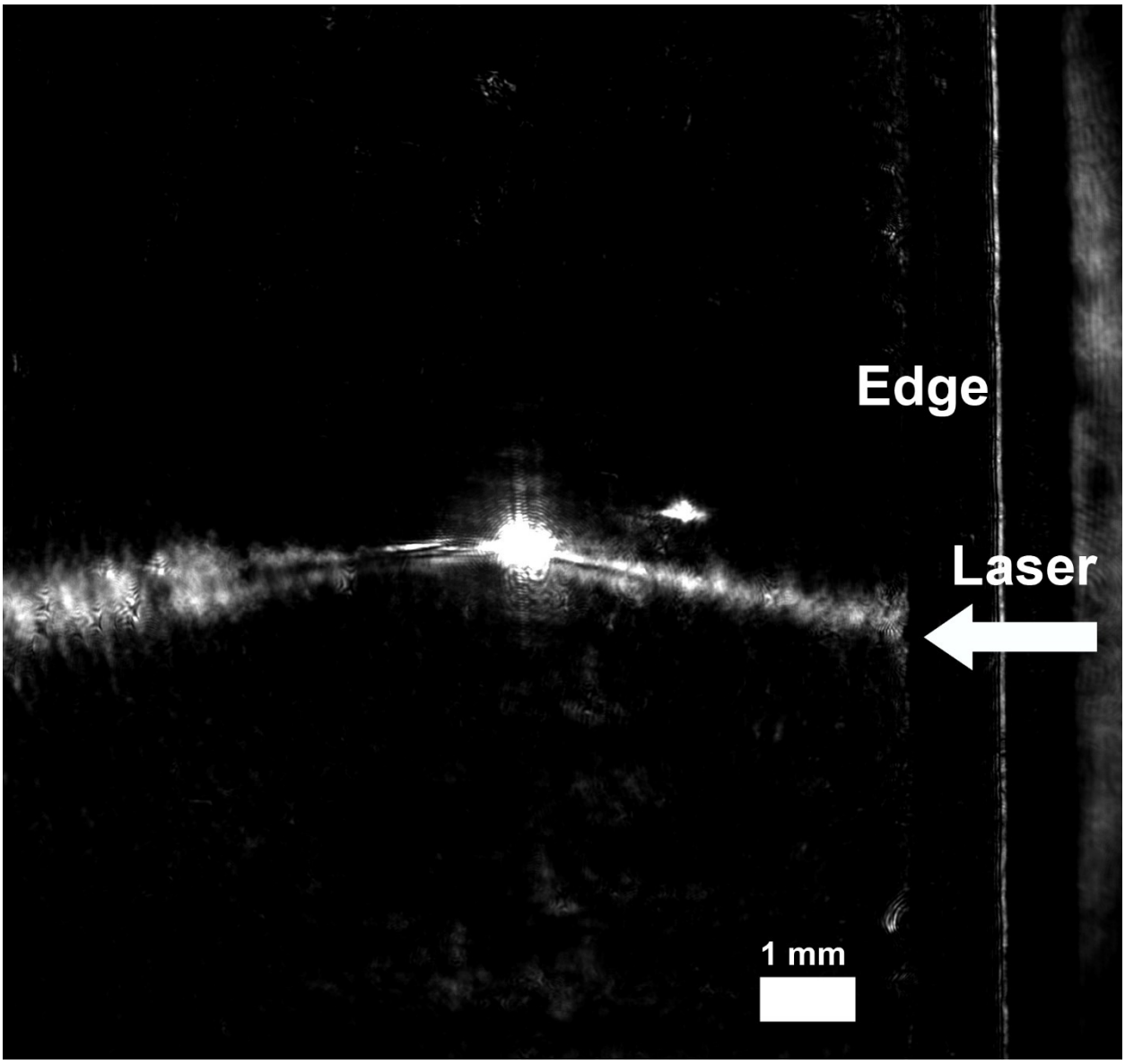

Figure S 11. Schlieren image for demonstrating the "thermal lens" effect at laser repetition rate of 1 kHz. The image was taken with a quartz cuvette of 10 mm optical path for optimal image quality.

6. Breakdown probabilities with and without ultrasound

Thus far, the enhancement from the NFU was directly observed; it can be attributed to both or either one of the two effects: the ultrasound can enhances each single pulse and result in an overall enhancement during the multiple lasing events within a collection period, and/or the ultrasound can improve the plasma ignition probability. To investigate the change in emission due to the presence of NFU, plasma images were taken. The maximal intensity from each plasma image were extracted and analyzed statistically in the form of histograms (*cf*. Figure S12). In total, 5000 axial profiles of the single-shot plasma at 5 kHz were recorded to ensure the statistical validity. The breakdown occurred 3160 times with ultrasound, whereas only 855 plasma events were recorded without it. Even with NFU, the breakdown probability was ~60% at the 5 kHz. It implied that the

breakdown can only occur after the energy accumulation of several laser pulses with our sub-mJ DPSS laser system. When breakdown occurred without ultrasound, the peak intensities exhibited a Gaussian distribution (*cf.* Figure S12, blue bars). Similarly, the distribution with ultrasound exhibited Gaussian feature as well; however, the center shifted towards a lower intensity (*cf.* Figure S12, red bars), which was ~1.4 times weaker than that without ultrasound. However, the overall higher ignition probability compensates for the lower emission intensity, with which a higher optical signal can be attained through the averaging or integrating. Additionally, the morphology of the plasma was also changed with respect to the presence of NFU and changing in repetition rate (*cf.* Figure S13). Detailed discussion can be found in SI, section 7.

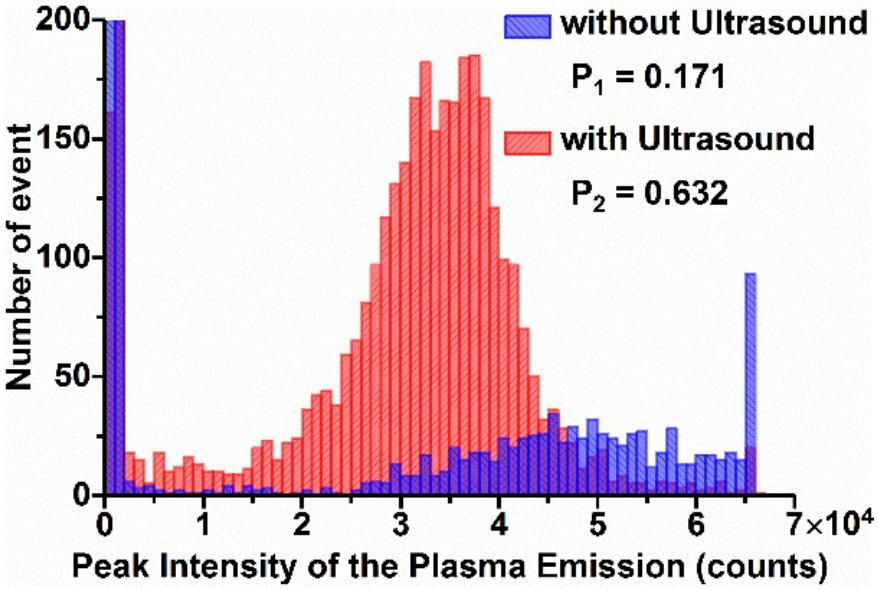

Figure S 12. Histograms of plasma intensity of individual pulses with and without the presence of ultrasound. The blue and red bars represent the statistical analysis without and with ultrasound, respectively. The "P" stands for breakdown probability. The y-axis was adjusted to show the plasma feature obviating the interference from the bin of 0 intensity, where no breakdown occurred.

7. Plasma-morphological studies under different conditions

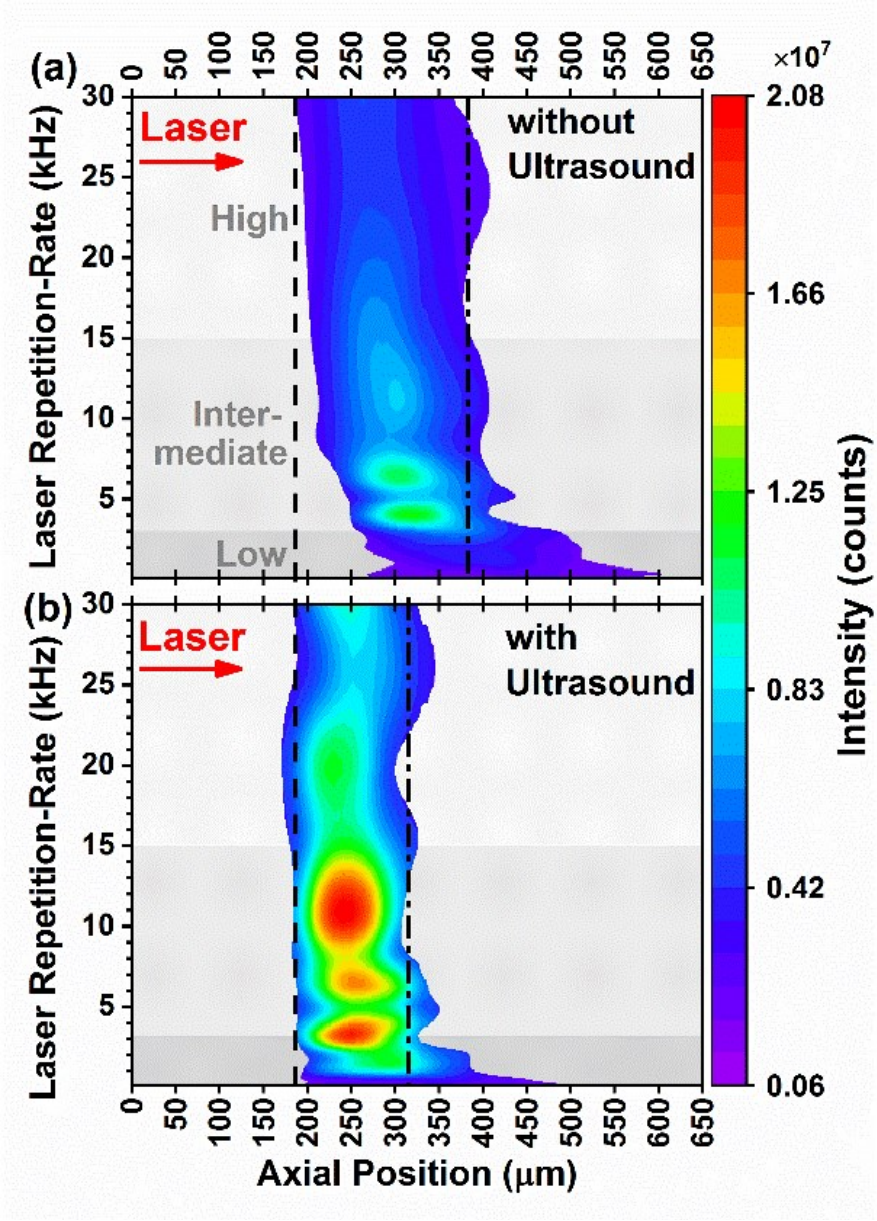

Figure S 13 Axial profiles (averaged over 1000 single shots) of the spectrally integrated plasma emission under different laser repetition-rates without ultrasound (a) and with ultrasound (b). In each acquisition, only one shot was recorded by disabling the "integration-on-chip". The overall emission intensities are denoted by the color-code. Note that pixels with intensities below a threshold (6×10^5 counts) are set to transparent. The dash and dash-dot lines denote the plasma geometric boundary. The gray scales in both (a) and (b) represent different bands of repetition, as labeled in (a). For better viewing, the data were first cubically interpolated into a 400×600 array. Thereafter, a two-dimensional boxcar filter of size 40×40 was used to smooth those images. The origin on the x-axis was arbitrarily chosen.

In order to investigate the plasma morphologies and volumes under different conditions, the plasma images were recorded by an iCCD (iStar DH 734i, ANDOR Technology Ltd., Belfast, UK) with a 20x-magnifying optical system. Specifically, the plasma was imaged by an objective lens (35 mm CCTV lens) and refocused by the same double lens (DL, effective focal length ~ 33 mm,

same as the one shown in Figure 1). The transmission distance in water was kept at 6.8 mm. The sample used here was the standard aqueous solution containing 600 µg /mL Ca^{2+} and µg /mL Na^{+}. The images were also recorded at the gate delay time of 28 ns and with a gate width of 1000 ns, which was the same as that of spectra recording. The exposure time of the iCCD was set as 0.011 s, with a 0/255 gain to avoid damaging the detector. The color bar was set according to the emission intensities in each image. Note that the plasma generated by the f=15 mm lens at the repetition-rate of 1 kHz was quite unstable, and too weak to be recorded. The background correction was performed by first setting the threshold value of 10% of the maximum intensity. Then the plasma volumes can be determined by the integration of the nonzero pixels (0.638 µm /pixel), assuming a rotational symmetry of the plasma with respect to the optical axis.

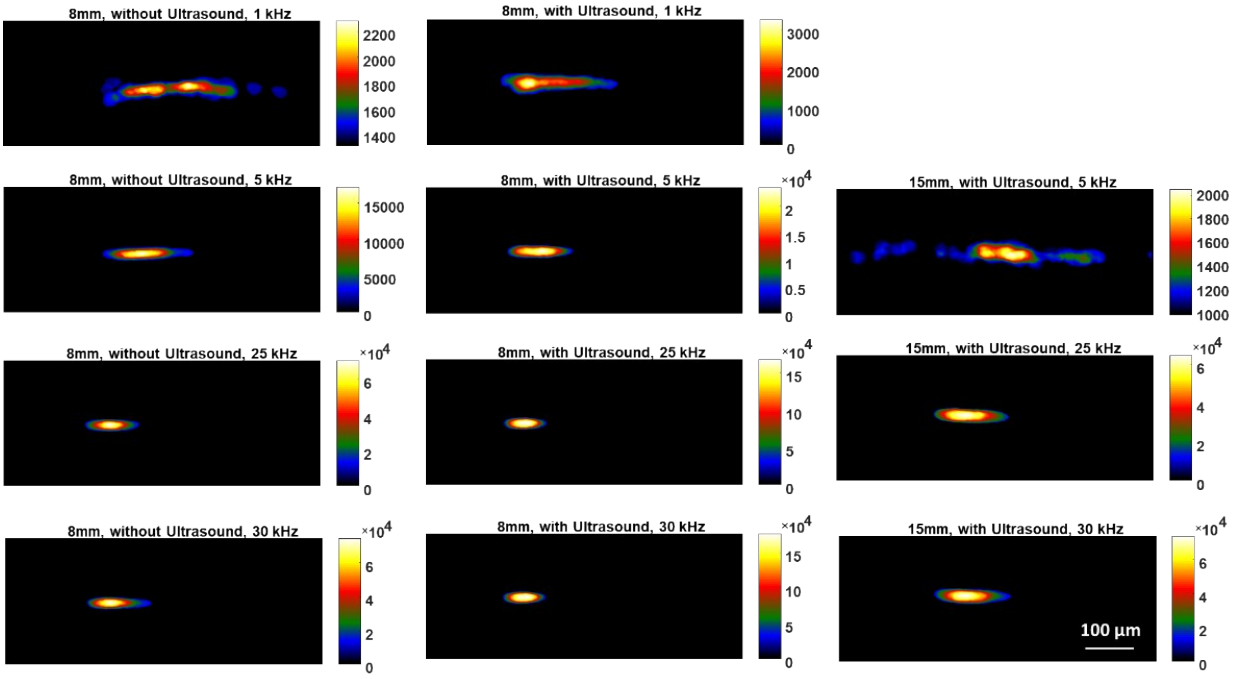

Figure S 14. Plasma images under the condition of f=8 mm lens without ultrasound (left), f=8 mm lens with ultrasound (middle) and f=15 mm lens with ultrasound (right), at the repetition-rate of 1 kHz, 5 kHz, 25 kHz and 30 kHz respectively.

To determine the plasma volume, the plasma volume is considered as cylindrically symmetric. From each image, the plasma perimeter was first determined. After normalizing each image (resulting in matrices containing elements ranging from 0 to 1), a threshold value of 0.6 was arbitrarily chosen as the threshold to define the plasma boundary. Thereafter, each column from individual images was evaluated to find the upper and lower boundaries. The difference was used to calculate the diameter of each pixel column. Based on the magnification factor (0.638 µ/pixel), the volume of vertical line was summed up to calculate the plasma volume.

8. Comparison of the signal-to-background ratios

To demonstrate the signal-to-background ratio (SBR) with respect to repetition rates, the emission line of atomic calcium (Ca I) at 422.7 nm was used as benchmark. The transmission distances in water of both lenses were kept at 6.8 mm. The spectra were recorded with the exposure time of 20

s, at a gate delay time of 28 ns and with a gate width of 1000 ns. The sample was a standard aqueous solution containing 600 μg /mL Ca^{2+} and μg /mL Na^{+}. In either case, the SBR increased near-monotonically with repetition rate (*cf*. Figure S15). Especially, at repetition rates above 15 kHz, the SBR obtained from the f=15 mm lens was almost doubled comparing to that with the f=8 mm lens (*cf*. Figure S15). The major reason can be attributed to the presence of continuum emission. In particular, longer focal lengths can be translated to "weaker" plasma, where continuum emission can be reduced or suppressed. Consequently, the SBR can be improved. Importantly, further decreasing the laser energy may result in unstable plasma ignition due to the reduced ignition probability. In this study, investigations regarding laser energy was not further made to seek for the optimal pulse energy to improve the SBR.

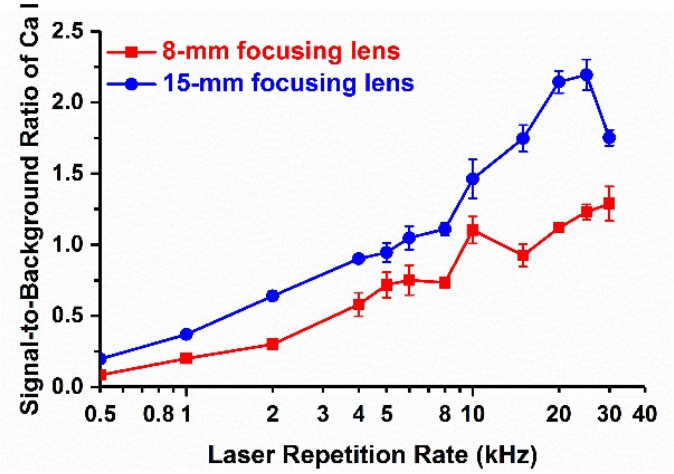

Figure S 15. Comparison of signal-to-background ratios obtained by the f=8 mm focusing lens and the f=15 mm focusing lens at different laser repetition rates.

9. Calibration curves of Ca^{2+} and Cr^{3+} in aqueous solutions

The calibration curves of Ca element were established both by the f=8 mm and the f=15 mm lenses, at the repetition rates of 1 kHz, 5 kHz, 25 kHz and 30 kHz, respectively. The transmission distances in water with both lenses were maintained at 6.8 mm. The sample solutions used here were $CaCl_2$ prepared in solutions of ten concentrations ranging from 7 μg/mL to 540 μg/mL. The spectra were recorded with the exposure time of 20 s, at a gate delay time of 40 ns and with a gate width of 1000 ns. The limit-of-detections (LoDs) were calculated with the 3σ/S criteria, where σ and S refer to standard deviation and sensitivity, respectively.

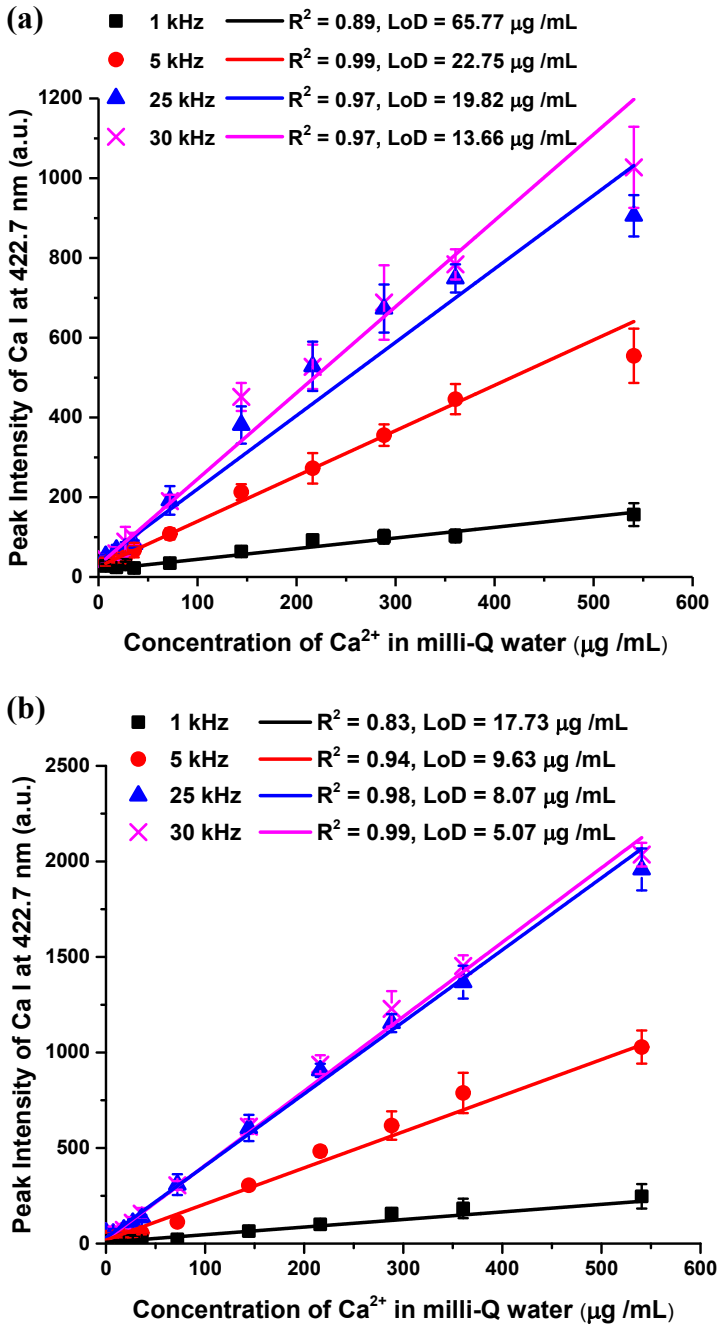

Figure S 16. Calibration curves of calcium in water solutions obtained by the f=8 mm focusing lens (a) and the f=15 mm focusing lens (b), at the laser repetition-rate of 1 kHz, 5 kHz, 25 kHz and 30 kHz, respectively.

The calibration curves of Cr (III) were further constructed by the f=15 mm lens, at the repetition rates of 5 kHz, 25 kHz and 30 kHz, respectively. The laser travels 6.8 mm in water. The sample solutions used here were $Cr(ClO_4)_3$ prepared in solutions of nine concentrations ranging from 57 to 180 µg/mL. The spectra were recorded with the exposure time of 20 s, at a gate delay time of 40 ns and with a gate width of 1000 ns.

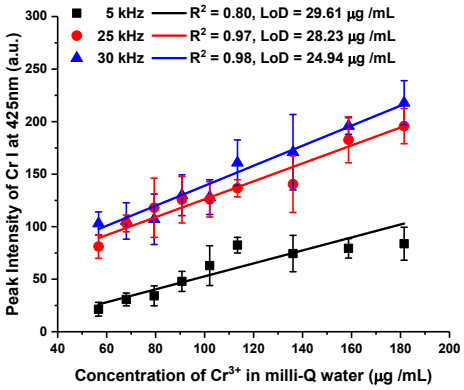

Figure S 17. Calibration curves of chromium in water obtained by the f=15 mm focusing lens at the repetition-rate of 5 kHz, 25 kHz and 30 kHz, respectively.

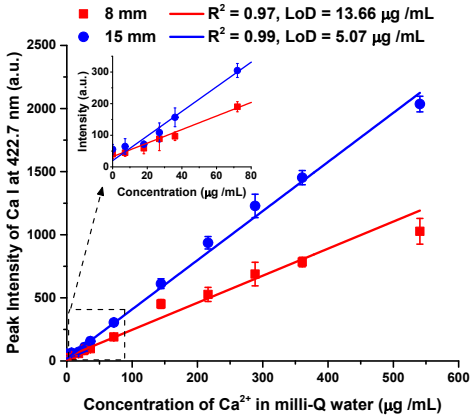

Figure S 18. Comparison of the calibration curves of calcium in water obtained by the f=8 mm focusing lens and the f=15 mm focusing lens, at the laser repetition rate of 30 kHz.

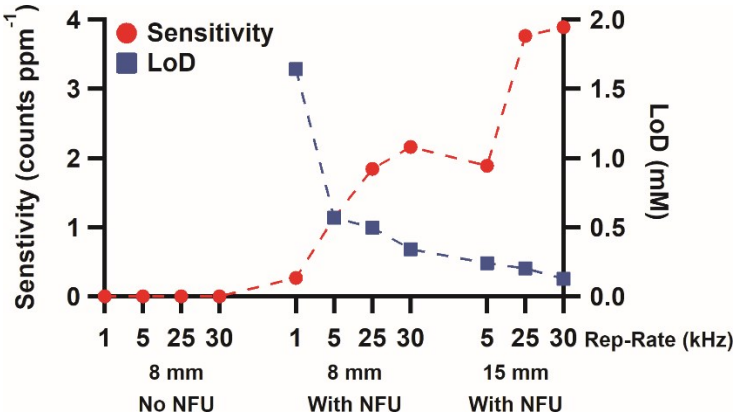

Figure S 19. Responses of sensitivity and LoD as a function of experimental parameters.

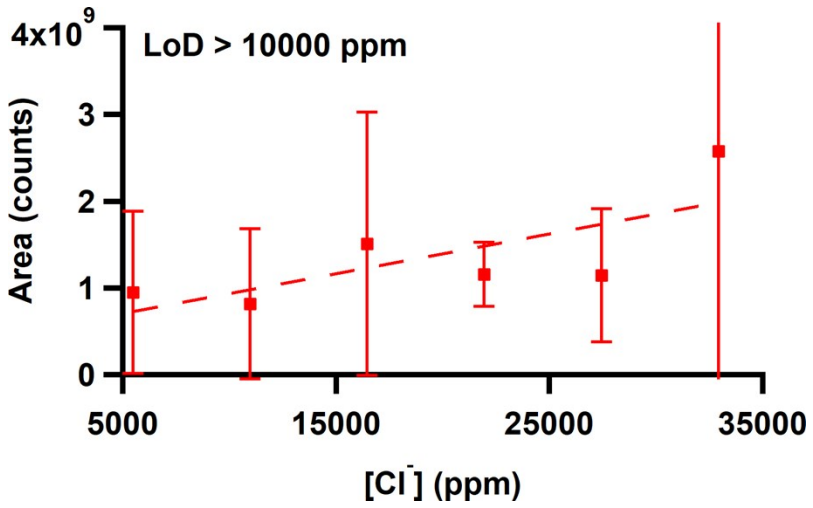

Figure S 20. Calibration curve of Cl without using O I as internal standard.